

Nanoscale mapping of point defects with 4D-STEM

Andrew Minor (✉ aminor@berkeley.edu)

University of California, Berkeley <https://orcid.org/0000-0003-3606-8309>

Sean Mills

University of California, Berkeley

Steven Zeltmann

University of California, Berkeley

Peter Ercius

Lawrence Berkeley National Laboratory <https://orcid.org/0000-0002-6762-9976>

Aaron Kohnert

Materials Science and Technology, Los Alamos National Laboratory

Blas Uberuaga

Los Alamos National Laboratory

Physical Sciences - Article

Keywords: high-resolution electron microscopy (HREM), Four-dimensional scanning electron microscopy (4D-STEM), electron-beam irradiation, vacancy concentration

Posted Date: July 1st, 2022

DOI: <https://doi.org/10.21203/rs.3.rs-1743810/v1>

License:  This work is licensed under a Creative Commons Attribution 4.0 International License.

[Read Full License](#)

Nanoscale mapping of point defects with 4D-STEM

Sean H. Mills^{1,2*}, Steven E. Zeltmann¹, Peter Ercius², Aaron A. Kohner³, Blas P. Uberuaga³,

Andrew M. Minor^{1,2*}

¹. Materials Science and Engineering, University of California at Berkeley, Berkeley, CA, USA

². National Center for Electron Microscopy, Molecular Foundry, Lawrence Berkeley National Laboratory, Berkeley, CA, USA

³. Materials Science and Technology, Los Alamos National Laboratory, Los Alamos, NM, USA

*Corresponding authors: seanmills@berkeley.edu, aminor@berkeley.edu

ABSTRACT

Vacancies are missing atoms in a crystalline material, and occur both at equilibrium (varying with temperature) and out of equilibrium such as when crystalline materials are damaged with radiation or corrosion. While we know of their importance, particularly regarding diffusive mechanisms, it is not straightforward to experimentally measure their concentration or to visualize them directly. Traditionally, measurements such as positron annihilation spectroscopy and to some degree X-ray diffraction can measure average concentrations, but generally lack the ability to visualize or quantify a heterogenous concentration of vacancies that can occur at the level of individual defects and microstructural features. Here, we present a method to map vacancy concentrations and their distribution with 1 nm resolution. Our method utilizes a Au thin film as a model to demonstrate the method via four-dimensional scanning transmission electron microscopy (4D-STEM) by correlating the differences between changes in lattice parameter and the volumetric thermal expansion during *in situ* heating experiments. The vacancy mapping methodology is also applied to non-equilibrium defects accumulated in pure Al via knock-on electron beam irradiation. Our method demonstrates the ability to map point defect concentrations in heterogeneous systems *in situ* with nanometer spatial resolution. The result is a technique that can provide direct measurements of vacancy concentrations at the level of individual defects in studies of materials in and out of equilibrium.

Keywords: high-resolution electron microscopy (HREM), Four-dimensional scanning electron microscopy (4D-STEM), electron-beam irradiation, vacancy concentration

A wide variety of important questions involving the thermophysical and structural properties of materials are tied to the equilibrium concentration of point defects. Vacancies are the simplest form of defects and are fundamental features shared by a variety of microstructural processes such as solidification, short range ordering in a crystal lattice, plastic deformation, and irradiation. The formation of point defects in solids was initially theorized by Frenkel et al.¹, who postulated that atoms become more mobile at elevated temperatures and overcome constraints imposed by the surrounding lattice. Atoms move to interstitial sites leaving behind a vacancy, which together are termed a ‘Frenkel pair’. The Wagner-Schottky model describes how vacancies remain in an otherwise perfect crystal when interstitial atoms leave their initial lattice positions to occupy free sites such as sample surfaces and other crystal imperfections². Modern theories suggest defects are directly created at these imperfections. Regardless of the source, the result is an equilibrium vacancy concentration that is required for plasticity mechanisms such as dislocation climb^{3,4} and diffusional creep⁵.

In transient conditions such as electrochemical cycling (eg- Li-ion battery cathodes or corrosion reactions in metals) or in extreme environments such as nuclear reactors, materials can evolve vacancy (and other point defect) concentrations substantially beyond what is considered a thermodynamic equilibrium. In these cases, ephemeral and heterogeneous vacancy concentrations impact mechanisms that degrade a material’s performance⁶. In these situations, the rate of point defect formation and migration are critical to determining the evolution of damage and rate of corrosion; however, the trends associated with varied temperature and irradiation dose are not intuitive, and a mechanistic understanding of the associated thermodynamics and kinetics remains poorly understood⁷. Therefore, a method for measuring

and spatially-resolving point defects such as vacancies is essential for the fundamental understanding of material behavior under complex damage modes.

Higher vacancy concentrations at elevated temperatures lead to an expansion in the sample volume, becoming most prominent as the temperature approaches the melting point of the crystal⁸. Therefore, the concentration of point defects can be effectively determined by measuring the difference between the volume expansion (or measured length if considering isotropic expansion) and the increase in the lattice parameter of a crystal. Foundational measurements by Simmons and Balluffi^{9–11} benchmarked this technique in bulk Al, Au, and Cu crystalline bar specimens by using optical dilatometry (to measure length change) and X-ray diffraction (XRD) (to measure lattice change).

Until recently, capabilities for directly determining the concentration of vacancies by way of measuring lattice parameter change have been limited to bulk techniques such as XRD¹⁰ as noted previously or positron annihilation spectroscopy (PAS)¹², where vacancies act as traps for positrons by which the vacancy accumulation can be quantified. Generally, these techniques provide volume-averaged properties (though recent depth-resolved PAS capabilities can provide some depth resolution^{13,14}). Recent developments in four-dimensional scanning transmission electron microscopy (4D-STEM) using high-speed direct electron detectors^{15,16} coupled with high resolution STEM now provide an opportunity for mapping lattice parameters at ~10 – 20 seconds time resolution with high precision¹⁷ and over a relatively wide field of view¹⁸. This offers the possibility of correlating defect content with microstructural features. 4D-STEM has been recently used to map stoichiometry¹⁹ and compositional changes^{20,21}, but has not been used to map primary vacancy concentrations where there is no change in chemical composition. Utilizing Au films in thermal equilibrium and irradiated Al out of equilibrium, we demonstrate a

state-of-the-art nanoscale point defect mapping technique and discuss fundamental vacancy-related mechanisms with respect to our experimental observations.

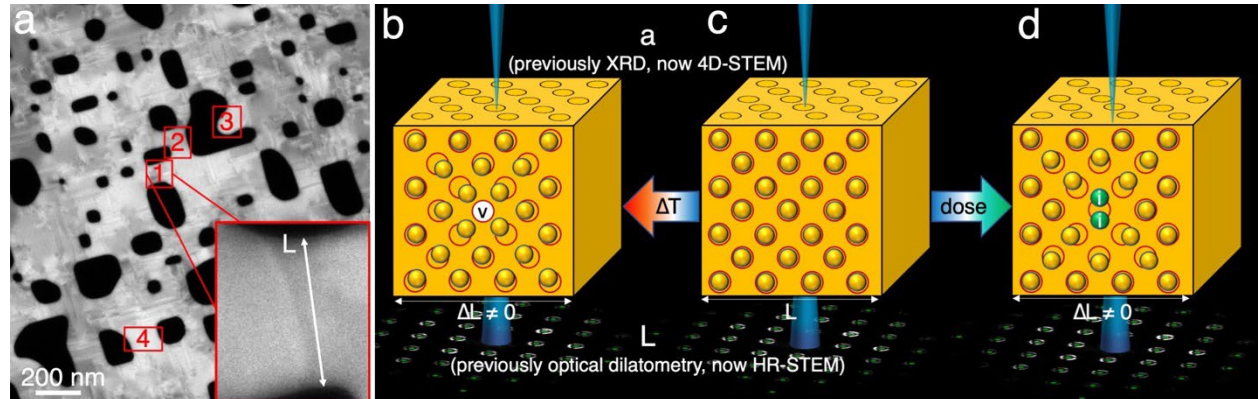


Fig. 1 | Schematic of 4D-STEM point defect mapping (a) Length measurements were conducted on HAADF-STEM images of most narrow point of ligament sections (red boxes) corresponding to the sample locations R1 – R4 where 4D-STEM measurements were taken *in situ* at each heating step. Lattice parameter measurement was derived from the median lattice parameters from collected 4D-STEM strain maps of the probed sample region. (b–d) Schematic illustrations of a nano-beam electron beam converged on a Au thin film. (c) Pure crystal at room temperature which is free of defects with a geometric dimension L. The d-spacing and lattice parameter are measured from a diffraction pattern collected for each scan position. (b) High temperature crystal containing a vacancy defect (white “v”) where the surrounding Au atoms are displaced in tension with respect to their unstrained lattice configuration (red circles). (d) Electron-beam irradiated crystal containing a split self-interstitial (green “i”) and here the surrounding Au atoms are displaced in compression with respect to their unstrained lattice configuration (red circles). The change in lattice parameter and d-spacing are measured via HR-STEM and 4D-STEM, respectively.

Figure 1 describes schematically how spatial maps, such as those shown in Figure 2 (a–d), are generated by way of 4D-STEM strain mapping technique to capture local changes in lattice parameter (indicated by the color-coded lattice parameter values) within the Au thin film. Recurring measurements were acquired *in situ* at sample regions R1 – R4 (red boxes in Figure 1a) during each temperature step (outlined by the heat treatment cycle in Extended Data 1 and in Methods). Figure 2 compares the initial 17 °C (a) measurement to the high temperature scans of the same region after heat treatment (800 °C (b) and 1000 °C (c)). The maps exhibit thermally

induced lattice expansion (1.23% and 1.60% respectively) that is consistent across the four scan regions. For example, the 1000 °C scan is a uniformly darker shade of blue compared to the 800 °C scan and corresponds to the maximum observed lattice parameter of 4.13 Å at the peak aged condition (1000 °C) just below the melting point (1063 °C) of pure Au. Rapid cooling of the sample (enabled by thermo-electric MEMS device) transpires in ~1 milli-seconds, similar to previous studies involving quenching (10^6 deg/sec) of bulk crystal^{22–24}. Overall, the microstructure remained consistent throughout the heating and cooling experiments, with minimal discernable changes in microstructural imperfections or features. Local fluctuations in strain associated with vacancies accumulated over the heating cycle were not resolvable in the HAADF-STEM images or the spatial maps due to the ~1 nm minimum probe size. Furthermore, there are no indications of heterogeneous defect formation or coarsening after multiple heating cycles. The resulting lattice parameter decreases to 4.067 Å after cooling (Figure 2d), comparable to measurement of the pre-heated condition, although not fully, and the discrepancy resolved later.

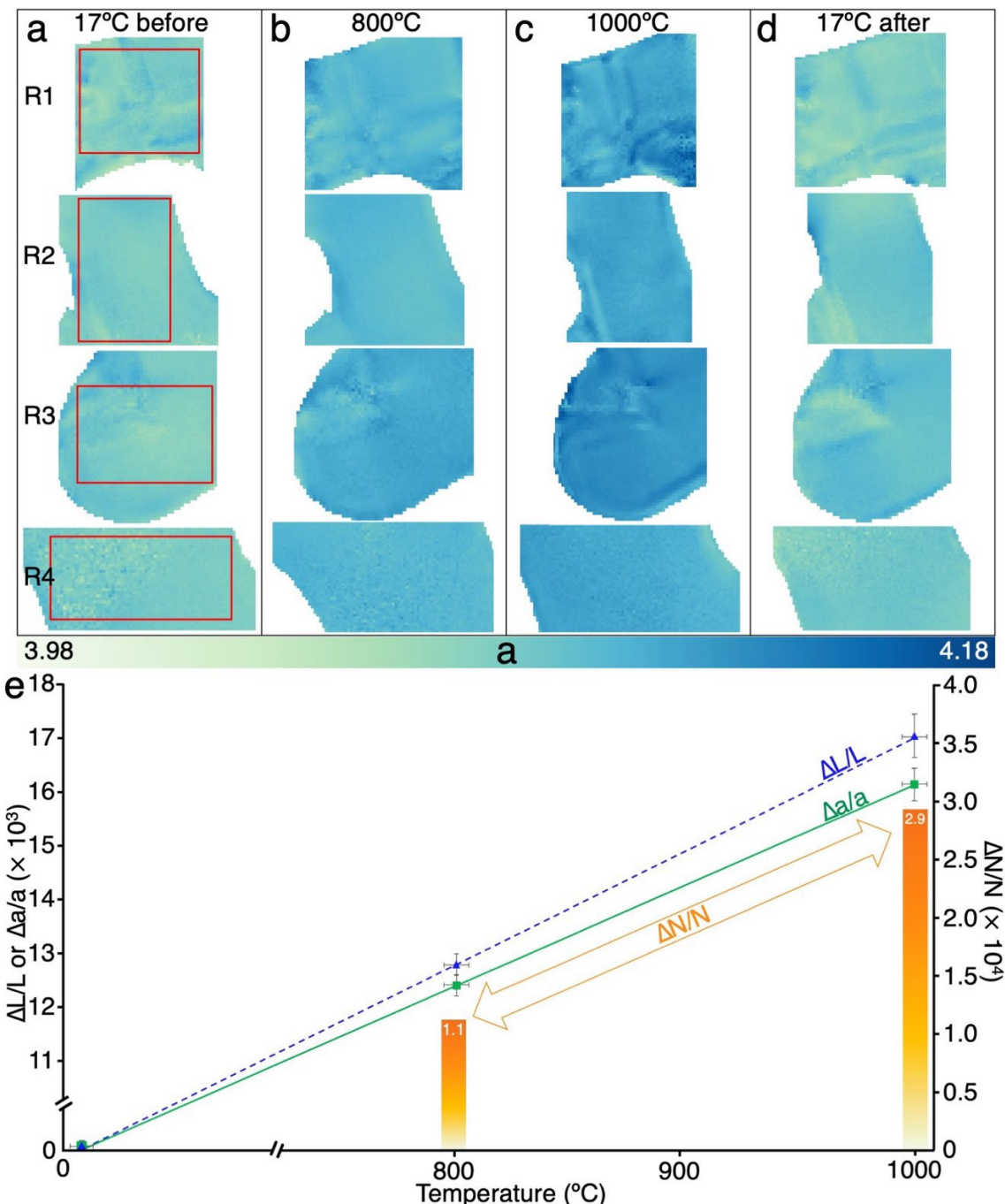


Fig. 2 | 4D-STEM lattice parameter mapping of thermally annealed Au. Four regions of interest are specified as R1 – R4, corresponding to the red boxes shown in Figure 1a. The average lattice parameter taken from scan positions in the red boxes in (a) is used as a reference to subsequent data sets taken from the same location. (a) 17 °C before heat treatment. (b) 800 °C during heat treatment. (c) 1000 °C during heat treatment. (d) 17 °C after rapidly cooling. (e) Length expansion (blue triangles, dashed blue line) and lattice parameter expansion (green squares, solid green line) of the pure Au thin film with respect to temperature (truncated to visualize measurements taken close to the melting point). Net added concentration of vacancies ($\Delta N/N$ noted by secondary vertical axis) is indicated (orange bars) for measurements taken at elevated temperature. All measurements include standard deviation for statistical comparison.

Figure 2e combines the lattice expansion $\Delta a/a (\times 10^3)$ from values collected at 17 °C (initial strain value used as a reference), 800 °C and 1000 °C that are averaged over the four sample regions (R1 – R4). Similarly, the average measured length expansion $\Delta L/L (\times 10^3)$ was extracted from careful measurement of the minimum dimension of these bridge-like features (between adjacent holes in the film) from HR-STEM images acquired at each temperature / time step. Both measurements are plotted with respect to temperature and trendlines are a linearly fitted to each dataset to illustrate the separation between the two measured variables with temperature. Previous work shows this divergence from linear thermal expansion becomes most noticeable while annealing temperatures approach the melting point (650 – 1063 °C) and the temperature range is presented accordingly from 700 – 1000 °C (peak aging temperature). This observed separation shares a direct relation with an increasing concentration of point defects¹⁰ as indicated by the orange bars plotted with respect to the secondary vertical axis ($\Delta N/N$). The larger change in sample dimension than lattice parameter indicates the measurements are detecting additional lattice sites, which are produced by forming vacancy defects and displacing those atoms to new sites on the surfaces. However, this is the first reported case where these trends (previously only performed with X-rays on a bulk crystal) are coupled with direct microstructural observations.

Interestingly, over both short (~minutes) and long (~days) timescales, complete lattice relaxation did not occur after each heating-cooling cycle. As Figure 3 describes, measurements of the same exact location taken approximately eight minutes apart or after a period of 30 days stored in air at ambient temperature showed a notable increase in lattice parameter and linear dilation with the number of heating/cooling cycles (see Extended Data Figure 1). Once brought up to temperature, the vacancies establish equilibrium of 2.91×10^{-4} within a millisecond or

less. When quenched to room temperature, the vacancies will be retained in the sample for a period of roughly 1 hour before beginning to escape to the surface. After 12-hours at 17 °C, defects are expected to deplete to concentrations $\leq 1.0 \times 10^{-6}$ which is below the resolution of our current measurement capabilities. When heated to 1000 °C, one would expect substantial diffusional creep under the influence of surface tension due to the large surface to volume ratio. The change in shape and lattice parameter after 30-days at room temperature shows the amount the material had crept at temperature, with that plastic deformation being largely retained when cooled back to 17 °C (in contrast to the residual vacancy population, which anneals out over this time). This leaves a large change in linear dilation, and a slight residual stress would explain the more modest lattice expansion. Considering the near-zero defect concentration after 30-days at room temperature, the creep relaxation and residual strain are the sole contributors to lattice expansion and linear dilation after this time. By normalizing this contribution to the measurements taken at the four heating cycle conditions, the vacancy concentration ($\sim 2 - 3 \times 10^{-4}$) and relaxation volume (reduced by 0.3 – 0.5 atomic volumes) are directly measured. Furthermore, the normalized measurement suggesting defects are largely retained in the short-term after four heating cycles is in alignment with the asymmetric behavior of defects upon heating (rapid accumulation) and cooling (slow depletion).

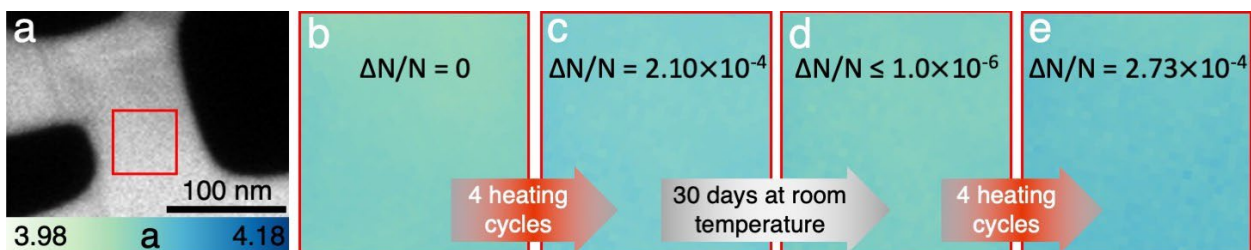


Fig. 3 | 4D-STEM lattice parameter mapping of Au post-quenching. (a) HAADF-STEM micrograph of the second sample location (R2). Room temperature 4D-STEM lattice parameter maps taken (b) at R2 immediately before, (c) immediately after four heating cycles, (d) 30 days after first experiment and (e) after a four additional heating cycles.

The above discussion shows how we can measure the vacancy content in equilibrated samples. To measure the formation and evolution of non-equilibrium defects, we demonstrate the mapping technique to defects accumulated in an electropolished Al sample by creating highly localized irradiation damage via the condensed 300 kV electron beam scanned at regular time intervals (60 – 120 seconds). This is equivalent to years of radiation exposure in practical engineering systems such as nuclear reactors, however, electron irradiation ($\sim 10^{-4} - 10^{-3}$ dpa/s) produces much higher dose rates compared to neutron irradiation ($\sim 10^{-7}$ dpa/s)²⁸. The knock-on electron beam damage method is applied to a $\leq 100 \text{ nm}^2$ square sample area while consecutive 4D-STEM datasets were acquired (Figure 4). Figure 4(a) highlights the resulting damage accumulation and the sequential lattice parameter maps suggest interstitial clusters on the order of 2 – 5 nm (light green locations in Fig 4b). The average lattice parameter associated with these electron irradiation-induced defect clusters is consistently lower than the global average lattice parameter of 4.048 Å which suggests these are comprised of interstitial-type defects, where the outward pressure e.g., a split interstitial structure (see Fig. 1) causes a compressive stress state on the surrounding lattice. Accumulation of vacancies is expected in conjunction with interstitial cluster growth. However, the volume of an interstitial is typically greater in magnitude than that of a vacancy, consistent with the compressive net effect in the measurement. In the ultrathin ($\leq 50 \text{ nm}$) electropolished sample, we posit that the un-irradiated sample volume surrounding the scan region imposes volumetric constraints on the irradiated volume and we can assume that $\Delta L/L$ is essentially zero. The reduction in lattice parameter coincides with an increase in point defect concentration ($\Delta N/N$), in the form of split interstitials and vacancies, with respect to the increase in number of 4D-STEM scans as shown in Figure 4(c), reaching a plateau after ~ 10 scans.

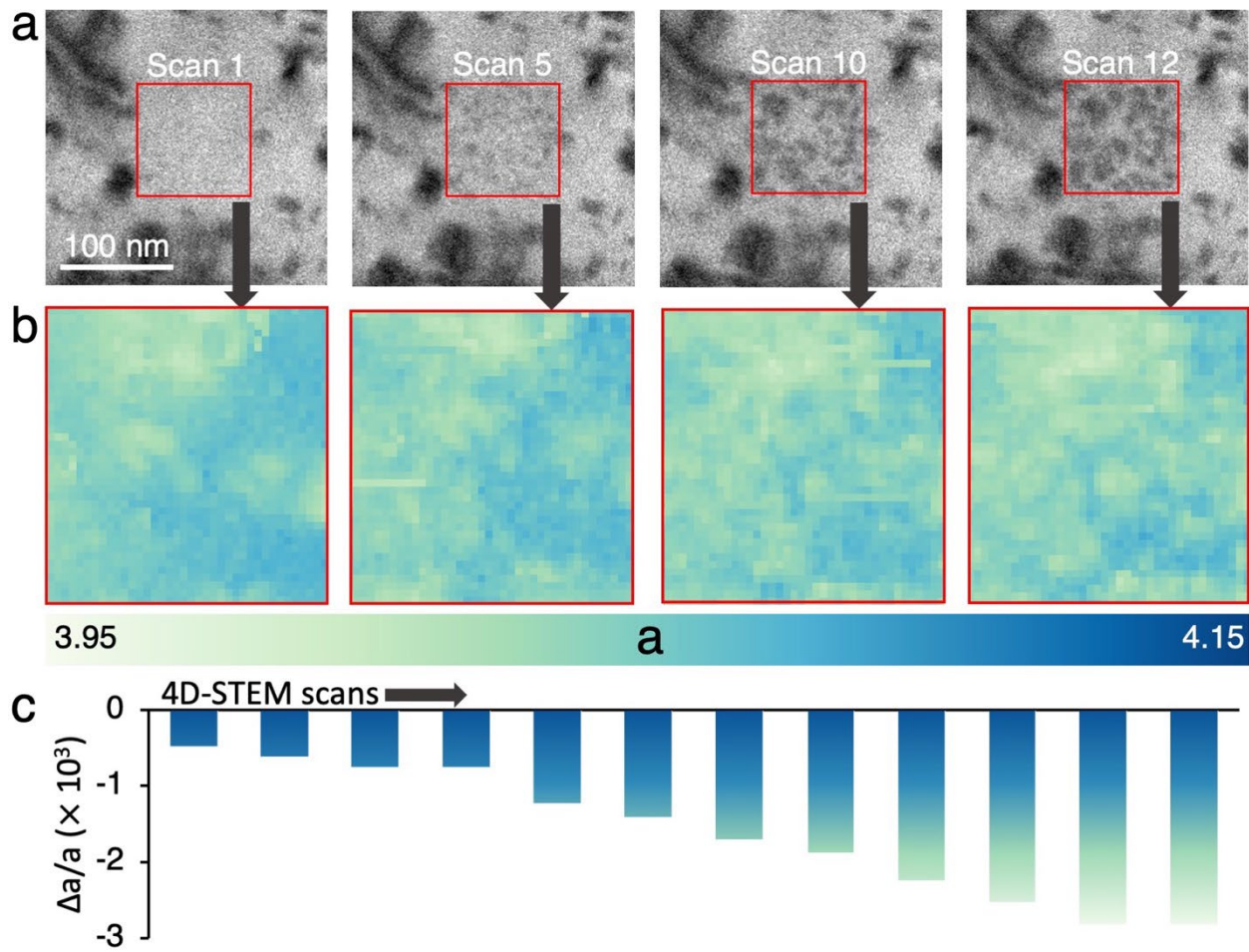


Fig. 4 | 4D-STEM defect accumulation in pure Al under direct electron beam exposure. (a) ADF-STEM images and lattice parameter maps of 4D-STEM scans taken within the corresponding red boxes. (b) 4D-STEM lattice parameter maps of data taken from red scan boxes in (a). Nano-scale irradiation defects are generated by direct exposure to condensed STEM probe. (c) Lattice parameter change $\Delta a/a (\times 10^4)$ plotted with respect to number of 4D-STEM scans (67,100 electrons \AA^{-2} per 4D-STEM scan).

Beyond the improvement in spatial resolution that our method has demonstrated for detecting changes in nano-scale defect concentration such as homogenous vacancies in thermally cycled Au and heterogeneous interstitial defects in irradiated Al, our measurements provide direct insight into the migration of point defects in a spatially resolved manner. First, given the retention of vacancies upon cooling and the minimal heterogeneous defects retained after each \sim 480 second cycle, we can estimate the migration energy of vacancies in Au using the minimum dimension (thickness) of the Au thin film. Previous estimates of the migration energy in Au have

shown a large discrepancy²⁹, to the point that it was not clear if we would be able to retain any vacancies in our quenched thin films for the minute long dwell period between rapid cooling and acquiring 4D-STEM scans. The migration of point defects for 3-dimensional random walk motion can be described via $r = d\sqrt{n}$ ²⁹. “d” is the nearest neighbor hop distance 2.9 Å and “n” is the total number of hops: $n = k \times t(\text{seconds})$ where “k” is the rate of hops. $k = Nv \times \exp\left(-\frac{E_m}{k_b T}\right)$ is a function of the migration energy (E_m), the value of which has been reported by several independent studies on Au. Matsukawa et al. reported $E_m = 0.85$ eV which results in little to no movement in the system²⁹. Contradictory evidence reports E_m as low as 0.62 eV, resulting in movement of several hundred nanometers, much larger than the distance required for a defect to escape from nearby surfaces of our thin films (≤ 25 nm). The energy range for pure Al is reported at 0.58 eV – 0.71 eV³⁰. Our results indicate that the migration energy to retain point defects is much closer to the Matsukawa findings in Au and 0.66 eV reported in Al³⁰ suggesting next to no defect movement considering the defects in both samples are retained during the room temperature dwell period between cycles (thermal or irradiation) in our experiments. Furthermore, retention of vacancy defects in the Au thin film is more apparent after multiple heating cycles as shown in Extended Data Figure 1. This change is several orders of magnitude higher than theoretical contributions from point defects, suggesting that other mechanisms discussed such as lattice diffusion creep^{5,31,32} and residual stress contributions are likely at play.

The 4D-STEM characterization method provides a robust qualitative description of the microstructure within a wide field of view and nano-scale resolution which makes it ideally suited to capturing heterogeneous point defect distributions. For example, the Au showed no indications of heterogeneous defect formation as the lattice parameter maps describe a

microstructure containing mono vacancies, randomly dispersed throughout the thin film that undergo no apparent coarsening after multiple heating cycles. The fundamental difference between the equilibrium behavior in Au and the non-equilibrium behavior in Al can be observed in the formation of defect clusters. In the irradiated regions of the pure Al sample, multiple passes of the condensed nanoprobe electron beam causes controlled formation of defect clusters that grow to 5 – 10 nm as shown in Figure 4. The readiness for visible clusters to develop rather than remain evenly dispersed as mono-defects indicates they are mobile interstitials in the Al sample that diffuse and coalesce. As individual defects agglomerate, they coarsen and, due to the size and the strains imposed on the neighboring atoms, act like sinks that attract interstitials that would otherwise escape the irradiated zone. Critically, when interstitials migrate to the clustered defects, they recombine with single vacancies located at the perimeter of the cluster and occupy that lattice position, annihilating both defects in the process. As the accumulation of vacancies and recombination with interstitials repeats over several exposures to the electron beam, quasi-steady-state is reached, and defect cluster growth becomes stagnant^{33–36}.

In conclusion, we demonstrated a method to map the concentrations of both equilibrium and non-equilibrium vacancy defects with nanometer spatial resolution and rapid time resolution. Similar to the classical work by Simmons and Balluffi^{9–11}, our method is generally-applicable in that all that is required are independent measurements of dilation and lattice parameters. However, in our case, the spatial resolution of the 4D-STEM also provides the ability to measure heterogeneous vacancy or interstitial concentrations, such as that shown in our irradiated regions of Al. Through this method, we experimentally benchmarked the migration energy of point defects in Au and compared equilibrium behavior to non-equilibrium super-saturations. We expect this methodology to be applied to basic and applied science applications in the future,

mapping vacancy concentrations in transforming materials such as battery cathode materials and in materials subjected to extreme environments of temperature, stress, and irradiation.

References

1. Frenkel, J. Über die Wärmebewegung in festen und flüssigen Körpern. *Z. Für Phys.* **35**, 652–669 (1926).
2. Silcox, J. & Hirsch, P. Direct observations of defects in quenched gold. *Philos. Mag.* **4**, 72–89 (1959).
3. Hirth, J. P., Lothe, J. & Mura, T. Theory of dislocations. *J. Appl. Mech.* **50**, 476 (1983).
4. Kassner, M., Kumar, P. & Blum, W. Harper–dorn creep. *Int. J. Plast.* **23**, 980–1000 (2007).
5. Nabarro, F. Steady-state diffusional creep. *Philos. Mag.* **16**, 231–237 (1967).
6. Grimes, R. W., Konings, R. J. & Edwards, L. Greater tolerance for nuclear materials. *Nat. Mater.* **7**, 683–685 (2008).
7. Zhou, W. *et al.* Proton irradiation-decelerated intergranular corrosion of Ni-Cr alloys in molten salt. *Nat. Commun.* **11**, 1–7 (2020).
8. Kraftmakher, Y. Equilibrium vacancies and thermophysical properties of metals. *Phys. Rep.* **299**, 79–188 (1998).
9. Simmons, R. O. & Balluffi, R. W. Measurements of equilibrium vacancy concentrations in aluminum. *Phys. Rev.* **117**, 52 (1960).
10. Simmons, R. O. & Balluffi, R. W. Measurement of equilibrium concentrations of lattice vacancies in gold. *Phys. Rev.* **125**, 862 (1962).
11. Simmons, R. O. & Balluffi, R. W. Measurement of equilibrium concentrations of vacancies in copper. *Phys. Rev.* **129**, 1533 (1963).
12. West, R. Positron studies of lattice defects in metals. in *Positrons in solids* 89–144 (Springer, 1979).
13. Hugenschmidt, C. Positrons in surface physics. *Surf. Sci. Rep.* **71**, 547–594 (2016).

14. Selim, F. Positron annihilation spectroscopy of defects in nuclear and irradiated materials-a review. *Mater. Charact.* **174**, 110952 (2021).
15. Ophus, C. Four-dimensional scanning transmission electron microscopy (4D-STEM): From scanning nanodiffraction to ptychography and beyond. *Microsc. Microanal.* **25**, 563–582 (2019).
16. Savitzky, B. H. *et al.* py4DSTEM: a software package for four-dimensional scanning transmission electron microscopy data analysis. *Microsc. Microanal.* **27**, 712–743 (2021).
17. Zeltmann, S. E. *et al.* Patterned probes for high precision 4D-STEM bragg measurements. *Ultramicroscopy* **209**, 112890 (2020).
18. Ozdol, V. *et al.* Strain mapping at nanometer resolution using advanced nano-beam electron diffraction. *Appl. Phys. Lett.* **106**, 253107 (2015).
19. Ding, Y. *et al.* Quantitative nanoscale tracking of oxygen vacancy diffusion inside single ceria grains by in situ transmission electron microscopy. *Mater. Today* **38**, 24–34 (2020).
20. Yang, Y. *et al.* 4D-STEM Imaging of nanostructural heterogeneities in Ni-20Cr after corrosion in molten salt. *Microsc. Microanal.* **27**, 2134–2135 (2021).
21. Yang, Y. *et al.* One Dimensional Wormhole Corrosion in Metals. *ArXiv Prepr. ArXiv220316312* (2022).
22. Kauffman, J. W. Quenching-in of lattice vacancies in pure gold. *Phys. Rev.* **97**, 555 (1955).
23. Ytterhus, J. A. & Balluffi, R. W. On the annealing of quenched-in vacancies in gold. *Philos. Mag.* **11**, 707–727 (1965).
24. Desorbo, W. Calorimetric studies on annealing quenched-in defects in gold. *Phys. Rev.* **117**, 444 (1960).
25. Schüle, W., Seeger, A., Schumacher, D. & King, K. Point defects in gold. *Phys. Status Solidi*

- 2**, 1199–1220 (1962).
26. Sonnenberg, K., Dedek, U., Ehrhart, P. & Schilling, W. On the interpretation of recovery stage III in gold: A comment on the paper of A. Seeger and W. Frank. *Radiat. Eff.* **77**, 269–272 (1983).
27. Sonnenberg, K. & Dedek, U. Migration energy of single vacancies in gold. *Radiat. Eff.* **61**, 175–178 (1982).
28. Karthik, C., Kane, J., Butt, D. P., Windes, W. & Ubic, R. In situ transmission electron microscopy of electron-beam induced damage process in nuclear grade graphite. *J. Nucl. Mater.* **412**, 321–326 (2011).
29. Matsukawa, Y. & Zinkle, S. J. One-dimensional fast migration of vacancy clusters in metals. *Science* **318**, 959–962 (2007).
30. Ono, K. & Kino, T. Migration energy of mono-vacancy in aluminum at high temperature. *J. Phys. Soc. Jpn.* **44**, 875–881 (1978).
31. Nabarro, F. & others. Report of a Conference on the Strength of Solids. *Phys. Soc. Lond.* **75**, 590 (1948).
32. Conyers, H. Diffusional viscosity of a polycrystalline solid. *J Appl Phys* **21**, 437–45 (1950).
33. Wiedersich, H. Evolution of defect cluster distributions during irradiation. in *Materials Science Forum* vol. 97 59–74 (Trans Tech Publ, 1992).
34. Rehn, L. & Wiedersich, H. Freely-migrating defects: Their production and interaction with cascade remnants. in *Materials Science Forum* vol. 97 43–58 (Trans Tech Publ, 1992).
35. Zinkle, S. & Singh, B. Analysis of displacement damage and defect production under cascade damage conditions. *J. Nucl. Mater.* **199**, 173–191 (1993).
36. Zinkle, S. J. & Farrell, K. Void swelling and defect cluster formation in reactor-irradiated

- copper. *J. Nucl. Mater.* **168**, 262–267 (1989).
37. Kino, T. & Koehler, J. S. Vacancies and divacancies in quenched gold. *Phys. Rev.* **162**, 632 (1967).
38. Pamato, M. G., Wood, I. G., Dobson, D. P., Hunt, S. A. & Vočadlo, L. The thermal expansion of gold: point defect concentrations and pre-melting in a face-centred cubic metal. *J. Appl. Crystallogr.* **51**, 470–480 (2018).
39. Dou, R. & Derby, B. Deformation mechanisms in gold nanowires and nanoporous gold. *Philos. Mag.* **91**, 1070–1083 (2011).
40. Horodek, P. Positron annihilation studies of irradiation-induced defects with swift heavy ions in gold. *Vacuum* **164**, 421–427 (2019).
41. Bustillo, K. C. *et al.* 4D-STEM of Beam-Sensitive Materials. *Acc. Chem. Res.* **54**, 2543–2551 (2021).

Methods

Materials and sample preparation

Au thin films were deposited on single crystal NaCl substrates using a custom thermal evaporator (NCEM, Molecular Foundry, LBNL). Bulk material was carefully weighed and placed in a tungsten crucible. The vacuum chamber was pumped down to a pressure of $< 10^{-6}$ mbar. The substrate was heated to 400 °C and the crucible was slowly heated up until it reached a temperature range of 180 – 200 °C (105 – 120 mA). Using a thickness monitor (Gatan) the substrate deposition rate was fixed at ~1-5 Å/second with subtle adjustments to the current to achieve a steady deposition of ~50 nm. Once the gold was fully deposited, the sample on salt substrate was held at 400 °C for 15 minutes before slow cooling to 17 °C. To remove the thin films from NaCl substrates they were carefully sectioned with a razor blade and partially submerged in DI water until the substrate fully dissolved, leaving the films suspended on the surface of the water. A looped wire tool was used to transfer the thin film via a water droplet to the ultra-thin carbon membrane section of a Protochips Fusion Select™ MEMS device. The film was carefully positioned over the exposed holey grid section of the membrane without contacting the electrodes on either side. The MEMS device was tested for a proper connection in the Protochips double tilt heating and biasing holder prior to the in-situ experiment.

In-situ heating and nano-diffraction electron microscopy

Au thin films were studied due to their ultra-thin geometry for HR-STEM characterization, resistance to oxidation and notable defect retention. The experimental design closely follows the differential thermal expansion method of measuring concentrations of point defects where thermally generated lattice-vacancy-type defects that compensate an equal

quantity of atoms can be measured¹⁰. The lattice parameter (measured by X-ray diffraction previously, but now by 4D-STEM¹⁵) and linear dilation (measured by filar micrometer previously, but now by STEM imaging) was studied at various elevated temperatures.

Measurement of additional atomic sites (vacancy production) as a function of increasing temperature is reproduced *in situ* on suspended Au thin films through implementation of a Protochips™ heating holder set-up to control sample heating with minimal drift. Moreover, custom patterned "bullseye" condenser apertures which improve the accuracy of 4D-STEM lattice parameter mappings¹⁷.

4D-STEM measurements were conducted on an FEI ThemIS image corrected microscope at 300kV. Nano-diffraction data was collected using a Gatan K2-IS (2k × 2k) detector at 400 frames per second. Each dataset contains a set of electron diffraction patterns taken at each scan position with a ~ 1 nm probe step size (1 milli-radian convergence angle). Approximately 80 × 80 scan positions were recorded from each region with a dwell time of 0.0025 seconds per frame. A custom 40µm patterned “bullseye” circular probe forming aperture was used to enhance the accuracy of 4D-STEM strain analysis by facilitating the identification of the center of diffraction discs¹⁷. A convergence angle of 3.20 milli-radians, spot size of 8, and diffraction pixel size of 0.16 Å⁻¹ was used in micro-probe lens configuration. The data was machine and software binned to 512 × 512 pixels to increase the signal to noise ratio before computational analysis. Data processing were performed using strain mapping scripts provided in the open source py4DSTEM software package¹⁶ and by a series of custom-made Python scripts.

In Figure 2, the average is taken from the distribution of measurements at each scan position across selected sample regions. The light green colored regions in Figure 2a-d indicate lattice positions where contraction is occurring (less than or equal to the reference region (red

box)). Conversely, darker blue colored regions indicate lattice positions where expansion is occurring. The lattice expansion $12.43(\times 10^{-3})$ and length expansion $12.79(\times 10^{-3})$ measured at $800\text{ }^{\circ}\text{C}$ corresponds to a net added concentration in vacancy sites of $1.08(\times 10^{-4})$. The maximum lattice expansion $16.18(\times 10^{-3})$ and length expansion $17.08(\times 10^{-3})$ measured at $1000\text{ }^{\circ}\text{C}$ correspond to a net added concentration in vacancy sites of $2.91(\times 10^{-4})$.

Au is an ideal material choice for study at varied temperatures and its capacity to produce and retain point defects at high temperatures is well reported. In pure Au, the binding energy is relatively high for the vacancies to overcome the migration energy at ambient temperatures ($30 - 125\text{ }^{\circ}\text{C}$, $E_B = 0.71 \pm 0.03\text{ eV}$ ³⁷). At moderate temperatures ($400 - 500\text{ }^{\circ}\text{C}$) this threshold reaches approximately 0.3 eV, where the mutual attraction between neighboring atoms is reduced, and minimal vacancies form in a pristine lattice^{22,23}. However, there is evidence of retained defects after heating/quenching and the measured concentration of accumulated vacancies ranges from $1.5 \times 10^{-6} - 5.0 \times 10^{-5}$ ^{22,23}. Approaching the melting point of most pure metals, the concentration of thermally generated vacancy defects reaches a peak ($10^{-4} - 10^{-3}$). These defects, dispersed evenly through an otherwise pristine lattice, promote a nonlinear effect on the specific heat and thermal expansivity approaching the melting point in Au ($600 - 1063\text{ }^{\circ}\text{C}$)^{8,38}. Moreover, non-equilibrium vacancy concentrations can accumulate in thin films, nano-wires and nanoporous structures during repeated material degradation processes such as heating/quenching², mechanical deformation³⁹, and irradiation damage⁴⁰.

The long-term retention of vacancy defects is explored by comparing lattice parameter maps acquired at the same sample location (R2) during two identical heating experiments which took place 30 days apart. This rest period at room temperature resulted in a lattice expansion of $0.29(\times 10^{-3})$ compared to the initial measurement, which is an 82% reduction compared to

$1.57(\times 10^{-3})$ measured after the fourth cycle of the first experiment. Moreover, the normalized linear dilation of the sample region decreased by 133% to $1.11(\times 10^{-3})$ after the 30-day rest which was followed by a 175% climb to $3.59(\times 10^{-3})$ after 4 additional cycles. The data (Extended Data Figure 1) is in close agreement with logarithmic relation $y = 0.6946 \ln(x) + 0.8689$ ($R^2 = 0.997$), where y is the lattice parameter change and x designates the thermal cycles.

Aggregated thermal effects like surface diffusion, residual stress, etc. are potential complications for extracting point defect density in the complex thin film geometry. By measuring these effects at multiple conditions, we can correct for them. As a basis for this correction, the lattice expansion and linear dilation defined as $\frac{\Delta a}{a} = (-\lambda)x_v + \varepsilon_{rel}^p + \varepsilon_{res} + \int \alpha(T)dt$ and $\frac{\Delta L}{L} = (1 + \lambda)x_v + \varepsilon_{rel}^p + \varepsilon_{res} + \int \alpha(T)dt$, respectively. ε_{rel}^p is creep relaxation, ε_{res} is residual strain, and $\int \alpha(T)dt$ is thermal expansion as a function of temperature and time. Using the experimental lattice expansion and linear dilation measurements taken after the 30-day room temperature hold (assuming $x_v = 0$ and $\int \alpha(T)dt = 0$), the net effect of the creep relaxation and residual strain are determined. These are subtracted from $\Delta L/L$ at the other room temperature measurements to normalize the defect concentration ($\Delta N/N$) as is presented in Figure 3.

Knock-on electron beam damage and in situ nano-diffraction electron microscopy

4D-STEM measurements were conducted on an FEI TitanX microscope equipped to do high-angle STEM tomography and operating at 300kV. Nano-diffraction data was collected using a Gatan Orius 830 (2k \times 2k) detector capable of collecting 30 frames per second. Each

dataset contains a stack of convergent beam electron diffraction (CBED) patterns taken at each scan position with maximum resolution equivalent to 1.6 nm probe size. Approximately 50×50 frame scan regions were recorded with a dwell time of 0.01 seconds per frame. A custom 70 μm patterned “bullseye” circular C2 aperture was used to greatly enhance the accuracy of 4D-STEM strain analysis by facilitating the identification of the center of diffraction discs ¹⁷. A convergence angle of 2.7 milli-radians, spot size 10, and camera length 195 mm was used in micro-probe lens configuration. With a measured screen current of 300 pA in this configuration, the total sum of electrons incident in a region of the sample, commonly known as the fluence (total dose), was determined at 67,100 electrons \AA^{-2} per 4D-STEM scan ⁴¹. Qualitative changes were observed after each scan which primarily consisted of heterogeneous irradiation defects which are interstitial in nature as reflected by the reduced lattice parameter (Extended Data Figure 3). The 4D-STEM data was machine and software binned to 512×512 pixels to increase the signal to noise ratio before computational analysis. Data processing and image analysis were performed using strain mapping scripts provided in the open source py4DSTEM software package ¹⁶ and by a series of custom-made Python and MATLAB scripts.

Applying the same general methodology to this unique microstructure benchmarks the use of 4D-STEM nano-diffraction and HR-STEM imaging for measuring defect concentrations and their spatial distribution which has not been possible with prior established techniques (XRD, PAS, etc.). Dislocation loops are known to form in pure Zn under certain beam energies, defects can form prior to nucleation of a dislocation loop in a pristine microstructure (Extended Data Figure 2). Heavier elements, such as Au have a relatively high threshold energy (1320 keV) and are therefore beyond the limit (300 keV) of the beam energy in modern transmission electron microscopes that could be used to produce permanent defects. A model metal sample was

necessary to showcase a mix of mono-vacancies and non-equilibrium vacancy-type defect clusters are present. Al has a much lower threshold energy (180 keV) that is well within the energy range of a condensed STEM probe, so it was selected for the knock-on damage experiment.

Data Availability

The authors would be happy to provide the data used for the preparation of this manuscript upon reasonable request to the corresponding author.

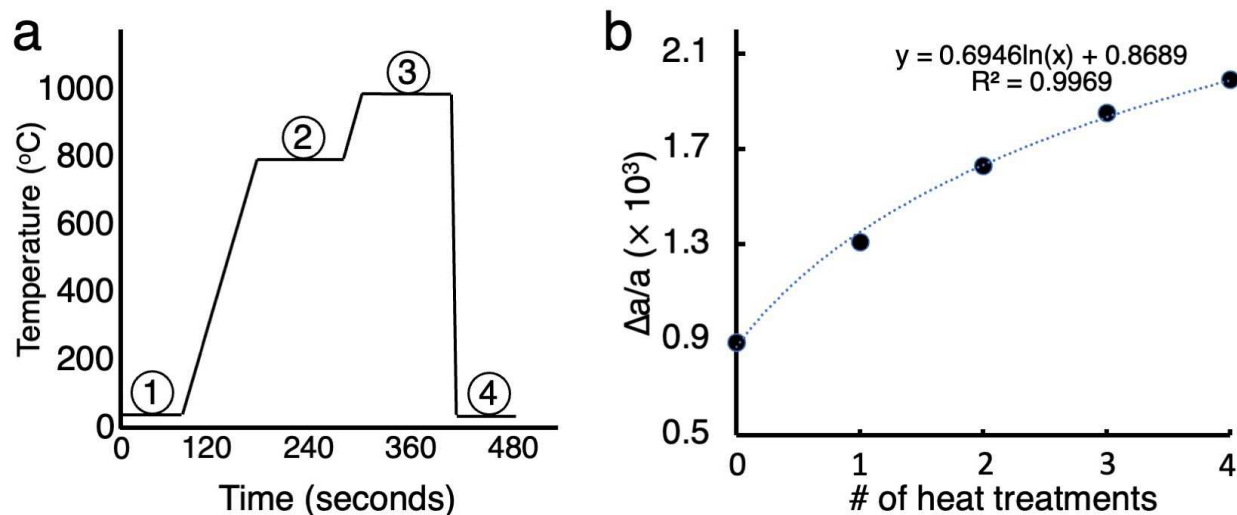
Acknowledgements

Primary support and funding for this work came from FUTURE (Fundamental Understanding of Transport Under Reactor Extremes), an Energy Frontier Research Center funded by the U.S. Department of Energy, Office of Science, Basic Energy Sciences. Work at the Molecular Foundry was supported by the Office of Science, Office of Basic Energy Sciences, of the U.S. Department of Energy under Contract No. DE-AC02-05CH11231. S.E. Zeltmann was supported by STROBE, a National Science Foundation STC funded under grant no. DMR 1548924.

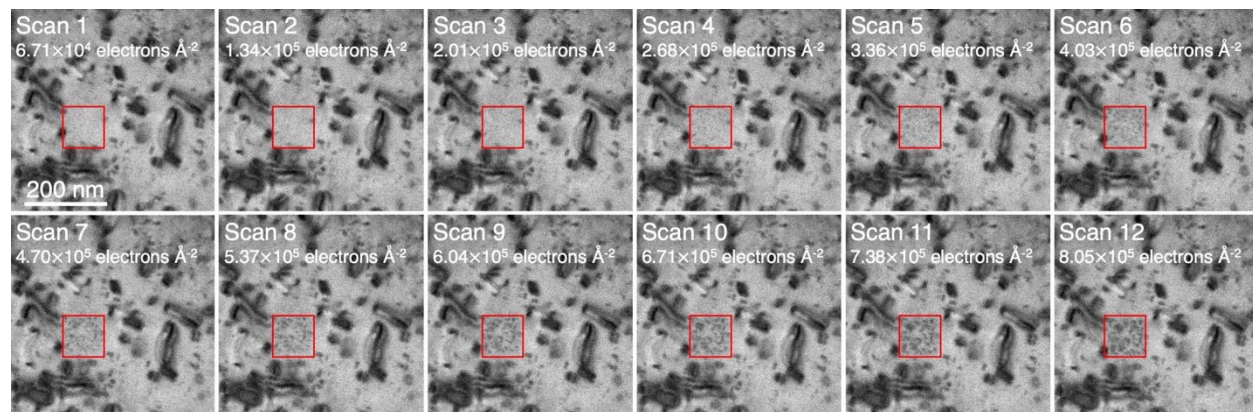
Author Contributions

S.H. Mills : conceptualization, methodology, data curation, formal analysis, writing: first draft, review and editing. **S.E. Zeltmann** : formal analysis. **P. Ercius** : data curation, formal analysis, writing: review and editing. **A.A. Kohnert** : interpretation of data. writing: review and editing. **B.P. Uberuaga** : interpretation of data, writing: review and editing. **A.M. Minor** : conceptualization, methodology, funding acquisition, writing: first draft, review and editing.

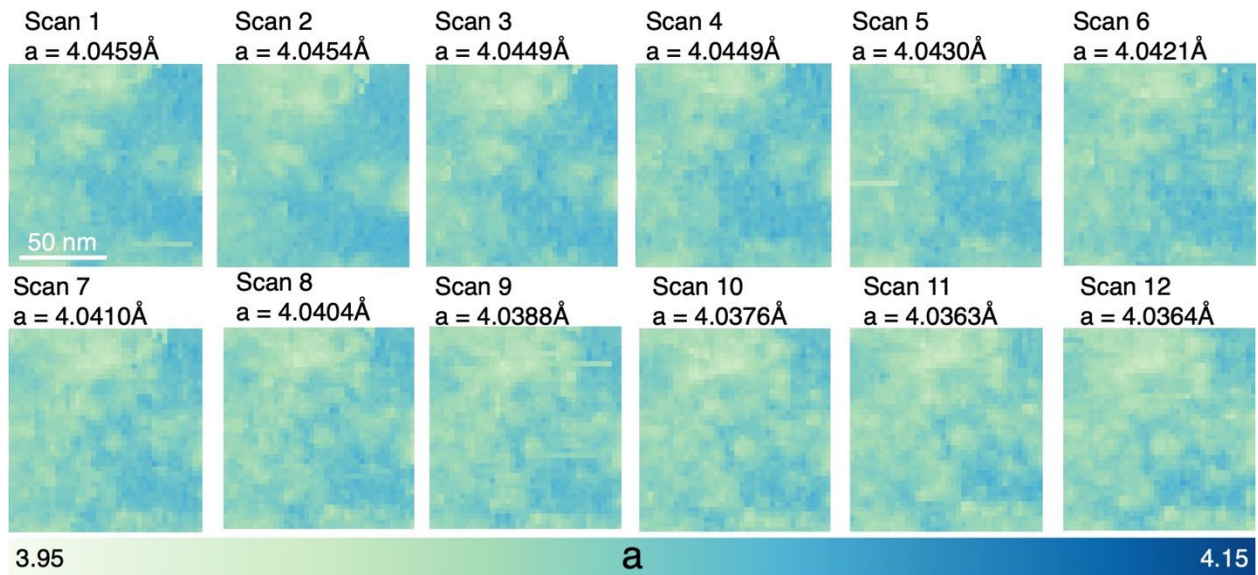
Extended Data



Extended Data Fig. 1. (Left panel) Temperature vs. time plot of a single heat treatment cycle. Heat treatment cycle consists of heating of ~ 10 °C/sec interrupted by holds at 800 °C and 1000 °C (peak temperature) for 4D-STEM data collection and followed by rapid cooling ($\sim 10^6$ °C/sec). 4D-STEM datasets collected at 4 indicated time intervals. This process was repeated over several cycles (Right panel) where lattice parameter change (reference taken before first heating cycle) was measured at 17 °C after each heating cycle. Logarithmic trendline indicates a close match with experimental values.



Extended Data Fig. 2. ADF-STEM images of Al sample exposed to 300kV electron beam irradiation during collection of consecutive 4D-STEM scans. Red boxes indicate electron irradiation exposed region where 4D-STEM scan is taken. Total dose in electrons Å⁻² is provided for each scan.



Extended Data Fig. 3. Lattice parameter maps generated from Al sample exposed to 300kV electron beam irradiation during collection of consecutive 4D-STEM scans. Qualitative maps track the nucleation and growth of several prominent point defect clusters (light green).